

Standard Article



Development of a fractal engine simulation model in a multidimensional simulation for the cold start process of a gasoline direct injection engine

International J of Engine Research
1–20
© IMechE 2023
Article reuse guidelines:
sagepub.com/journals-permissions
DOI: 10.1177/14680874231174272
journals.sagepub.com/home/jer

Delong Li<sup>\*</sup>, Jinghu Hu<sup>\*</sup>, Matthew Hall and Ron Matthews

#### **Abstract**

A fractal engine simulation (FES) sub-model was integrated into three-dimensional simulations for modeling turbulent combustion for a gasoline direct injection (GDI) engine. The FES model assumes that the effects of turbulence on flame propagation are to wrinkle and stretch the flame, and fractal geometry is used to predict the surface area increase and thus the turbulent burning velocity. Different formulas for the four sequential stages of combustion in SI engines are proposed to account for the changing effects of turbulence throughout the combustion process. However, most prior studies related to the FES model were quasi-dimensional simulations, with few found in multi-dimensional studies, and none under cold start conditions or stratified charges. This paper describes how the model was implemented into multidimensional simulations in CONVERGE CFD, and what the formulas are in the four sequential stages of combustion in SI engines. The capabilities of the FES model for simulating the cold start cases, under the conditions of the dramatically changing engine speed and mixture stratification in a complex engine geometry, are presented in this study. The FES model was able to not only simulate the steady-state cases with constant engine speed, but also predict the in-cylinder pressure traces in all four cylinders for the very first firing cycle with transient engine speed, and gave good agreement with the experimental measurements under these extremely transient conditions. The uncertain maximum fractal dimension was chosen as 2.37 in this research, and a simple linear correlation with engine speed was used to obtain the coefficient used in calculating the kernel formation time which controls the so-called combustion or ignition delay.

### **Keywords**

Fractal engine simulation (FES) model, gasoline direct injection (GDI) engine, cold start, three-dimensional simulation, turbulent combustion

Date received: 20 December 2022; accepted: 14 April 2023

## Introduction

The gasoline direct injection (GDI) engine has many benefits over the port fuel injection (PFI) engine, including higher efficiency and thus better fuel economy and improved performance, and has been developed rapidly since it first appeared in the market (e.g. Environment Protection Agency<sup>1</sup>). However, the cold start emissions remain a key challenge for GDI engines due to the stringent 2025 U.S. emissions standards for light-duty vehicles. It has been reported that more than 90% of hydrocarbon (HC) emissions originate from the first 2 min of engine operation when the temperature of the catalysts is low.<sup>2</sup> In the cold start process, the very first firing cycle deserves special attention, as

most HCs come out during this cycle, and then gradually decrease during subsequent cycles, as shown by prior cycle-resolved cold start experiments<sup>3,4</sup> by our research team. The fuel rail pressure (FRP) is much lower when the engine is first started during the very

Walker Department of Mechanical Engineering, University of Texas at Austin, Austin,  $\mathsf{TX}$ ,  $\mathsf{USA}$ 

\*Co-first authors

## Corresponding author:

Matthew Hall, Walker Department of Mechanical Engineering, University of Texas at Austin, 204 E. Dean Keeton St. C2200, Austin, TX 78712, USA.

Email: mjhall@mail.utexas.edu

first firing cycle, and the cold walls in the engine make the fuel film evaporation very slow, resulting in more fuel injected for compensation and leading to more mixture stratification in the cylinder. The engine speed will increase sharply after ignition during this cycle if misfire does not occur.

All of these transient behaviors add difficulties to the combustion modeling. Simulating the flame propagation associated with the kernel formation and early flame growth becomes more critical. These early stages of combustion usually happen before the engine speeds up, leading to more actual time spent per crank angle. Thus, the chemical reactions during the several crank angles right after the start of ignition are important to consider and can affect the predicted cylinder pressure traces (both phasing and magnitude) and the indicated mean effective pressure (IMEP). Rapidly increasing engine speed results in increasing turbulence in the cylinder, which compensates for the reduced time for the chemical reactions, affecting the overall combustion rate. Moreover, the highly stratified mixture, caused by the injection in the compression stroke along with the low wall film evaporation rate, results in quite nonuniform flame speeds in the combustion chamber. To solve all of these potential problems in accurately modeling cold start, the fractal engine simulation (FES) model is what we used for the cold start simulations.

The FES model solves the turbulent combustion in a more physically meaningful way, and assumes that flame wrinkling and stretch are the dominant effects of turbulence on flame propagation in spark ignition (SI) engines. It uses fractal geometry to account for the flame surface wrinkling, and then is able to predict the turbulent flame speeds based on the instantaneous local fractal dimension and stretched laminar flame speed. The FES model has been tested and verified from different experimental measurements, and proves a promising model for the turbulent combustion category of laminar flamelets, 5.6 wherein the flames within SI engines fall for most operating conditions.

Before carrying out the FES model, we tried to use the SAGE detailed chemistry model.<sup>8</sup> The SAGE model tracks the flame front propagation by solving the local chemical kinetics, and has been successfully applied to engine simulations for many different conditions. However, there is a limited number of papers on simulating different cylinders for the very first firing cycle in the cold start. Our research group has studied the effects of different transient behavior under such conditions in a previous study,9 but only for the first cylinder to fire. When we applied the same settings of the SAGE model to the other cylinders for the very first firing cycle, the mismatch was especially evident in the initial combustion, characterized by very rapid heat release rates, as shown in Appendix A. The problem possibly arose due to the effects on the flame of different turbulence levels for different cylinders and even for the same cylinder at different crank angles (due to the rapidly changing engine speed within a cycle). Ravindran and Kokjohn<sup>10</sup> extensively explored the use of the SAGE model in the laminar regime for cold-start conditions, and found that it presented challenges, under-predicting the flame propagation speeds, also noting that further study was needed to evaluate the turbulence-chemistry interactions in other regimes. Consequently, we decided to explore the implementation of the FES model - a model physically predicting the turbulence-flame interaction and also a model we have been working on for years - into the multi-dimensional simulations for cold start. It should be noted that the G-equation model, as presented by Ravindran et al., 10,11 appropriately modified, has been demonstrated to simulate cold-start conditions well for the portion of the cold start following the initial transient period where the engine is operating at constant speed in catalyst heating mode. However, it is not the focus of this paper.

Fractal geometry was first introduced for simulating turbulent premixed combustion by Gouldin<sup>12</sup> in 1987. Gouldin pointed out that the fractional increase in multiple scales of wrinkling could be predicted employing fractal concepts, and results within 30% were shown, assuming a constant fractal dimension (D) of 2.37, when he compared his fractal predictions with previous experimental measurements<sup>13,14</sup> in a combustion bomb for five different fuels in air and for an extremely broad range of turbulence conditions. However, it was soon shown that the fractal dimension increases with increasing turbulence intensity in burner-type flames. 15-17 Santavicca et al. and coworkers<sup>18</sup> developed a relationship between the fractal dimension, the turbulence intensity (u'), and the unstretched laminar flame speed  $(S_L)$  based on the physical arguments that the mechanism for producing flame wrinkles is turbulent convective motion, which is characterized by u', and that this wrinkling is opposed (i.e. small scale wrinkles are smoothed) by the combustion process, which is characterized by  $S_L$  Their model represents a weighted average of these effects between two limiting fractal dimensions. For a premixed flame propagating in a laminar flow field, the flame surface will be smooth, and the fractal dimension will equal the topological dimension, D = 2.0. Various theories have been proposed for the upper limit of the fractal dimension in a high Reynold's number flow field, with values ranging from 2.33 to 2.41 (e.g. Gouldin, Hilton, and Lamb, 1988<sup>19</sup>; Francke and Peters, 1990<sup>20</sup>) and Santavicca and coworkers chose 2.35 for their model. In 1992, our research team showed<sup>21</sup> that their model for the fractal dimension of turbulent flame surfaces predicted the measured fractal dimensions of flames in SI engines<sup>22</sup> within 3.6%: A modified version of their model for the fractal dimension was used in the present FES model, as discussed

Following the research discussed above, much work, for example, <sup>23–41</sup> has been focused on the turbulent combustion in SI engines, along with experimental measurements. Most of the models developed using FES were quasi-dimensional models, where the zero-dimensional

thermodynamic models were applied up to the time of ignition, and two zones, burned and unburned (these two zones are often subdivided into boundary layers and isothermal cores, and a crevice zone is sometimes added as well), were utilized for the duration of the combustion process. Only a few studies can be found focused on multi-dimensional simulations using the ideas of fractal geometry, Zhu et al.'s research<sup>28</sup> for example, where she proposed a multi-dimensional numerical model that accounted for the premixed flame propagation in a homogenous charge SI engine with a nearly axisymmetric geometry. Due to the fact that the FES model physically describes the interaction between the turbulence and the flame surface area, it can be fully extended to three-dimensional simulations for a GDI engine, where the instantaneous local mixture properties and the instantaneous local turbulence parameters are to be used to calculate the spatial and temporal fractal dimensions and burning velocities in the cylinder. Thus, in this paper, we will demonstrate the full capabilities of the FES model to handle complex conditions, including the irregular engine geometry, the mixture stratification in the cylinder, and the rapidly changing engine speed.

The remainder of the paper is structured as follows. The details related to the FES model will be presented first, including what correlations are used to describe the different phases in turbulent combustion in SI engines, how we integrated the FES model into the three-dimensional combustion simulation in CONVERGE CFD, and the correlations for the laminar flame speed and flame thickness we used in the FES model. The effect of kernel formation time on the combustion intensity is shown next. Finally, the experimental validations for both steady state and cold start conditions are provided. Pressure traces and heat release curves for all four cylinders are included for the very first firing cycle under cold start, including the CA50, the magnitude and location of peak pressure, and the IMEP.

## **Details of the FES model**

Different combustion regimes are usually classified by two dimensionless numbers: the Damköhler number (Da, the ratio of a characteristic time for turbulence to that for a laminar flame) and the Karlovitz number (Ka, the ratio of a characteristic residence time within a laminar flame to the time scale for dissipation of turbulence kinetic energy in the smallest turbulence scale). In the laminar flamelet regime, Da is very large and Ka is very small. In other words, the chemistry is usually fast enough in laminar flamelets that the flame lies within a very thin layer, for which the thickness is smaller than the smallest length scale of the turbulent flow (the Kolmogorov length scale,  $\eta$ ). This situation occurs for most operating conditions of an SI engine. In essence, the term "laminar flamelet" means that the effects of turbulence in the combustion chamber are to wrinkle and stretch the flame surface, thus increasing the

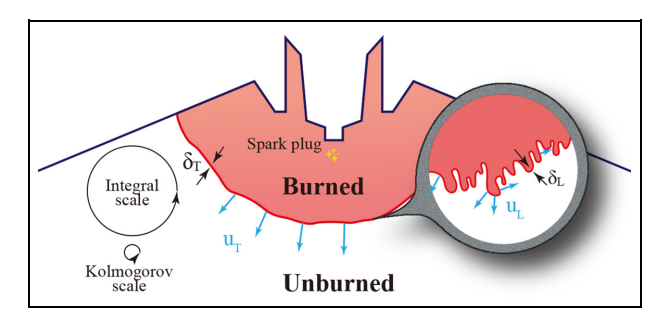


**Figure 1.** Schematic of a turbulent premixed flame in an SI engine:  $\delta_T$  and  $\delta_L$  are the turbulent and laminar flame thickness, respectively;  $u_T$  and  $u_L$  are the turbulent and laminar flame speed, respectively.

surface area and increasing the flame speed, as shown in Figure 1.

To relate the turbulent flame speed to the laminar flame speed, one will have:

$$\frac{u_T}{u_L} = \frac{A_T}{A_L} \tag{1}$$

where  $A_T/A_L$  is the fractional increase in flame surface area due to the effects of turbulence. As initially recognized by Gouldin, fractal geometry can be used to quantitatively model the increase in flame surface area:

$$\frac{u_T}{u_L} = \frac{A_T}{A_L} = \left(\frac{L_{max}}{L_{min}}\right)^{D-2} \tag{2}$$

where D is the fractal dimension, which quantitively characterizes the degree of the flame wrinkling;  $L_{max}$  is the maximum flame wrinkling scale, which is larger than the integral length scale ( $L_i$ ), as in equation (3) shown in previous studies, <sup>17,19</sup> or equals the instantaneous flame radius in the early combustion phase when the flame radius is still smaller than  $L_i$ ;  $L_{min}$  is found to be larger than the Kolmogorov length scale ( $\eta$ ) in the aforementioned studies, as shown in equation (4).

$$L_{max} = C_{max}L_i \tag{3}$$

$$L_{min} = C_{min} \eta \tag{4}$$

where  $C_{max} > 1$  and  $C_{min} > 1$ ;  $C_{max}$  and  $C_{min}$  are two scaling parameters and treated as constants.

Then the problem turns into how we choose appropriate values for the flame wrinkling scales (or turbulence length scales) and the fractal dimension. To help obtain the different scales in the FES model, a detailed k- $\epsilon$  model for turbulence is used in the present model, where the instantaneous and spatially-resolved Kolmogorov scale  $(\eta)$  and integral scale  $(L_i)$  can be calculated via:

$$\eta = \left(\frac{\nu^3}{\varepsilon}\right)^{\frac{1}{4}} \tag{5}$$

$$L_i = \frac{u^{\prime 3}}{\varepsilon} \tag{6}$$

where  $\nu$  is the laminar kinematic viscosity of the unburned mixture,  $\varepsilon$  is the dissipation rate of turbulence kinetic energy, and u' is the turbulence intensity. The relationship between the maximum-to-minimum flame wrinkling scales and the scales of turbulence is dependent upon the specific phase of the combustion process, as discussed in the following section. When the instantaneous local flame wrinkling scales and fractal dimensions are determined, the instantaneous local turbulent flame speed can be calculated, and thus the three-dimensional simulation can be then carried out.

## Models in different phases of combustion

The combustion in an SI engine is generally divided into four phases: kernel formation, early flame growth, fully developed turbulent combustion, and end of combustion. Models for each phase are discussed below.

Phase 1: Kernel formation. A small flame kernel is first initialized by the spark plug and time is required to wrinkle the flame kernel in this phase.<sup>23</sup> During this wrinkling delay, the flame is assumed to grow at the instantaneous stretched laminar flame speed. The duration  $(t_{KF})$  in this phase is described as the initial kernel diameter  $(D_{ign})$ , the spark gap) over the eddy turnover velocity  $u_{KF}$ , the latter of which is determined from the characteristic equation (7):

$$\varepsilon = \frac{u^{\prime 3}}{L_i} = \frac{u_{KF}^3}{D_{ien}/2} \tag{7}$$

$$t_{KF} = C_{KF} \frac{D_{ign}}{u_{KF}} \tag{8}$$

where the local instantaneous value of  $\varepsilon$  within the spark gap is obtained from the turbulence model and  $C_{KF}$  is a dimensionless adjustable constant,<sup>23</sup> which decreases with increasing engine speed, and no delay is needed for engine speeds over 1500 RPM. The effect of  $C_{KF}$  will be shown later in this research.

The flame kernel is initially quite small and thus it is assumed that it grows at the instantaneous stretched laminar flame speed  $(u_L)$ , which is related to the unstretched laminar flame speed  $(S_L)$  by a stretch factor  $(\kappa)$ .

$$u_L = S_L * \kappa = S_L (1 - \{\kappa_E + \kappa_S\}) \tag{9}$$

where  $\kappa_E$  and  $\kappa_S$  are two stretch factors associated with flame expansion and turbulence strain, respectively, the details of which can be found in Chin et al. 's research.<sup>21</sup>

For now, the empirical equations and parameters, with  $C_{KF}$  calibrated against experimental data, are needed in calculating the ignition delay time (ignition either occurs or there is a misfire; "ignition delay" refers to the very short period when the pressure rise due to the initial heat release is so small that it is somewhat difficult to measure). However, a predictive model is

preferable, and one can then determine how the spark transitions to turbulent combustion for any working condition. Efforts are being made by our research team to integrate a fully predictive kernel formation submodel into the engine simulations, to account for the effects of arc breakdown and the subsequent interactions of the spark with the surrounding turbulent flow.

Phase II: Early flame growth. The transition to this phase occurs at the end of  $t_{KF}$ . During this stage, the flame radius  $(r_f)$  is still smaller than the integral length scale  $(L_i)$ , so the flame cannot be affected or wrinkled by all scales of turbulence. Thus, the largest size of eddy which can wrinkle the flame is limited by the size of the flame, and a characteristic velocity  $(u_{EFG})$  is used instead of u' to describe the wrinkling effect of turbulence. The fractal dimension is expressed by:

$$D = 2.37 \frac{u_{EFG}}{u_{EFG} + S_L} + 2.0 \frac{S_L}{u_{EFG} + S_L}$$
 (10)

Similar to the eddy turnover velocity in the kernel formation phase,  $u_{EFG}$  is calculated by:

$$\varepsilon = \frac{u^{\prime 3}}{L_i} = \frac{u_{EFG}^3}{r_f} \tag{11}$$

In order to allow a smooth transition to the next combustion stage (fully developed turbulent combustion) shown below,  $C_{min}$  equals 1.0 in equation (4). Thus, the ratio of flame wrinkling scales during early flame growth is:

$$\frac{L_{max}}{L_{min}} = \frac{r_f}{\eta} \tag{12}$$

Phase Ill: Fully developed turbulent combustion. The transition to this phase occurs when the flame radius equals the integral length scale. Most of the fuel is burned in this phase, and as soon as the flame grows larger than the integral length scale, it is exposed to the full range of turbulent eddy sizes. As shown in Wu's paper<sup>23</sup>, it is reasonably assumed that the ratio of flame wrinkling scales can be expressed as:

$$\frac{L_{max}}{L_{min}} = \frac{L_i}{\eta} \tag{13}$$

where  $C_{max}$  and  $C_{min}$ , in equations (3) and (4), are almost at the same level that they cancel out. That is, even though  $L_{max} > Li$  and  $L_{min} > \eta$ , the ratio of the maximum-to-minimum flame wrinkling scales equals the ratio of the maximum-to-minimum scales of turbulence. Finally, the fractal dimension is calculated based on the relationship developed by Santavicca, Liou, and North, <sup>18</sup> and later shown by our research team to yield excellent agreement<sup>21</sup> with fractal analysis data for premixed flames within an SI engine<sup>22</sup>:

$$D = 2.37 \frac{u'}{u' + S_L} + 2.0 \frac{S_L}{u' + S_L} \tag{14}$$

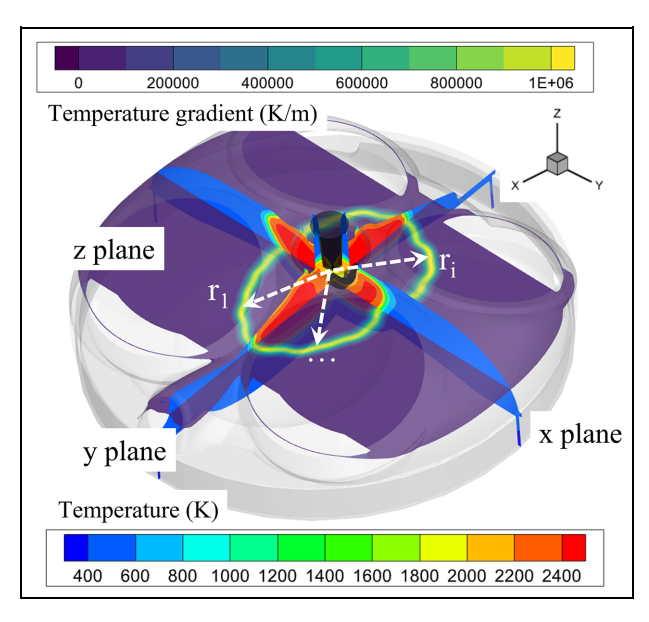


**Figure 2.** A schematic figure to show how to calculate the flame radius.

Different coefficients can be found as the first constant (the maximum possible fractal dimension of a wrinkled surface) in expressing the fractal dimension with values ranging from 2.33 to 2.41. <sup>19,20</sup> Santavicca et al. who developed equation (14), used 2.35. However, 2.37 is used in the present research, and excellent agreement will be seen later when compared with the experimental measurements.

Phase IV: End of combustion. The peak pressure occurs when all of the surfaces of the flame have entered the thermal boundary layer alongside the walls in the cylinder, which indicates the combustion in the engine enters the last phase. The combustion process gradually slows down due to the wall cooling effects. For the cold start case, the wall wetting begins to evaporate faster than before this phase, due to a high near-wall gas temperature. However, the intensity of combustion decays and much of the late-evaporated fuel cannot be burned out, which may introduce more engine-out hydrocarbon emissions.

## Flame radius calculation

When the flame grows to the same size as the integral length scale, the combustion phase will transition to the stage of fully developed turbulent combustion. Prior to that, the combustion is not progressing as fast, since the flame cannot be wrinkled by all scales of turbulent eddies. Thus, it is essential to know the size of the flame radius at each crank angle increment. However, the shape of the flame is irregular for a GDI engine, even more than for a PFI engine, due to the fuel stratification and mixture inhomogeneities in the cylinder.

A schematic figure is presented in Figure 2 to show how we estimated the radius of the flame in the

three-dimensional simulations of this research. Shown on x and y cut planes is the contour for temperature, and the z plane is the magnitude of the temperature gradient. High temperatures are seen on the x and y planes near the spark plug, indicating the burned zone, and a low temperature range appears outside, indicating the unburned zone. These two zones are separated by a yellowish circle on the z plane, where the magnitude of the temperature gradient is very high. The flame front would be represented where all these circles on different z planes with very high temperature gradients are connected.

In any direction starting from the center of the spark plug, the cell with the highest magnitude of temperature gradient can be found. On the same z plane, we can calculate the average distance  $(r_z)$  from those cells to the spark plug. Then the maximum value of  $r_z$  among different z planes is defined as the flame radius in this study, as shown in equation (15):

$$r_f = \max_{z} r_z = \max_{z} \left( \frac{1}{N} \sum_{i=cell\_1}^{cell\_N} r_{z\_i} \right)$$
 (15)

## Integration with three-dimensional simulations

The  $\alpha$ - and  $\beta$ - transformations  $^{42}$  are used to integrate the FES model, as shown in Zhu's research,  $^{28,43}$  into the three-dimensional simulations in the present research. The user-defined functions (UDF) in CONVERGE allow us to make changes to the default model in CONVERGE, and then have the simulations run as expected in the FES model discussed above. It will be briefly demonstrated next how the  $\alpha$ - and  $\beta$ - transformations function.

The standard k- $\epsilon$  turbulence model in a Reynolds-Averaged Navier-Stokes (RANS) model is used to model the fluid motion before the time of ignition. Then the combustion chamber will be divided into two zones when combustion happens: the standard k- $\epsilon$  model is used to simulate the turbulent flow for the unburned region outside the flame, and the  $\alpha$ - and  $\beta$ - transformations are to be used to solve for the required properties with the flame zone based on corresponding formulas in different phases of the FES model.

In these transformations, the laminar mass, momentum, and energy diffusivities are all scaled by a factor of  $\alpha * \beta$ , and the chemical reaction rate is scaled by another factor of  $\alpha/\beta$ , so that the computed flame speed  $(u^*)$  and computed flame thickness  $(\delta^*)$  are increased by the factor  $\alpha$  and  $\beta$ , respectively:

$$u^* = \alpha S_L \tag{16}$$

$$\delta^* = \beta \delta_L \tag{17}$$

where  $S_L$  is the unstretched laminar flame speed and  $\delta_L$  is the laminar flame thickness. In essence, a scaled laminar flame is solved in the flame zone, instead of solving a wrinkled turbulent flame directly.

**Table 1.** Numerical settings in the simulations.

Process	Details	Settings				
Mesh generation	Fixed embedding	Base grid size: 4 mm. Fixed embedding: level 2 for the				
· ·	Adaptive mesh refinement (AMR)	entire cylinder; level 3 for spray; level 5 for ignition. AMR: level 3 using the sub-grid (SGS)-based type for				
	remement (, a my	temperature and velocity. Boundary AMR included as				
		well, for valves as an example. Overall cell number:				
		200,000–2,000,000 at different CADs.				
Boundary layer	Standard wall	Law-of-the-wall assumption for velocity in the log-law				
	treatment	region.				
Heat transfer	Fixed temperature	Room temperature for cold start, and 90 °C for steady state.				
Fuel	Iso-octane					
ruei	iso-octane	Laminar flame speed from chemical kinetics in Liu et al., <sup>45</sup> provided in the following section.				
Spray breakup	Modified KH-RT	Model constants: KH size constant $B_0$ : 0.6; KH time				
	model	constant $B_1$ : 7.0; RT size constant $C_{RT}$ : 0.6; RT time constant $C_{\tau}$ : 1.				
Spray-wall interaction	Wall film model	Critical Weber number We <sub>crit</sub> : 5.0; Critical value for				
	O'Rourke model	splashing $E_{crit}^2$ : 3330; Fraction splashed: 1.0.				
Vaporization	Drop vaporization	Frossling model				
•	Film vaporization	Uniform temperature model				
Turbulence	Standard k-ε model	Different coefficients: $C_{\mu}=$ 0.09, $C_{\varepsilon 1}=$ 1.44,				
		$C_{\varepsilon 2}=$ 1.92, and $C_{\varepsilon 3}=$ 0.327.				
Ignition	Source model	A spherical shape of source delieved to the spark plug				
5		gap.				
Combustion	FES model	Details elaborated in the present paper.				

Combined with the FES model discussed above, the  $\alpha$  and  $\beta$  values can be determined for different phases of combustion. In the fully developed turbulent combustion phase, for example, the coefficient  $\alpha$  is:

$$\alpha = \frac{u^*}{S_L} = \frac{u_T}{u_L/\kappa} = \left(\frac{L_{max}}{L_{min}}\right)^{D-2} * \kappa = \left(\frac{L_i}{\eta}\right)^{0.37 \frac{u'}{u' + S_L}} \kappa$$
(18)

The coefficient  $\beta$  is:

$$\beta = \frac{\delta^*}{\delta_L} = \frac{\delta_T}{\delta_L} \tag{19}$$

where  $\delta_T$ , the turbulent flame thickness, is assumed as 0.6 mm for the cold-start cases, which came from the previous three-dimensional simulation results using the SAGE combustion model in CONVERGE (details are provided in Appendix B);  $\kappa$  is the flame stretch factor from equation (9).  $S_L$  and  $\delta_L$  are calculated based on the correlations shown in the next section, as functions of temperature, pressure, and equivalence ratio. After the transformations are implemented, the three-dimensional turbulent flame can be modeled when the instantaneous spatial values of  $\alpha$  and  $\beta$  in the flame zone are used.

## Other settings

Iso-octane was used as the fuel for the reaction kinetics, and considering the importance of vapor pressure in cold start simulations, it was changed to that of gasoline having a Reid vapor pressure (RVP) of 7, with true vapor pressure (TVP) calculated from Moshfeghian's correlations.<sup>44</sup>

The standard wall function was used in the three-dimensional simulations as the wall treatment. The wall temperatures were set constant and the same as the coolant temperature monitored in the experiments: ambient temperature for the cold-start cases, and 90°C for the steady-state case below. A film vaporization model was included as well to account for the slow film evaporation process under cold-start conditions.

For the sake of brevity, the models and settings in the simulation are all listed in Table 1.

For the cold-start simulation runs of the very first firing cycle, two full cycles have been simulated, with the first one simulating the dummy cranking cycles in the experiments for engine synchronization, and the second one simulating the combustion process. We have also tried using two cranking cycles in the simulation before ignition, but there was no difference in the pressure trace for the firing cycle. For the steady-state simulation runs presented in this paper, four cycles were simulated: the first cycle simulated only the cranking process, providing the background flow fields; the second and third cycles were both firing cycles, designed to obtain the residual fraction in the cylinder and also to achieve the convergence of the turbulent flow fields in the engine; the fourth cycle was also the firing cycle, and results from this cycle were provided in the present paper.

Parameters	Pressure range	Equivalence ratio	U [m/s]	$lpha_{L}$	$oldsymbol{eta}_{L}$	$\gamma_{L}$
S <sub>L</sub> [m/s]	Low (I-I2bar)	I	4100	-0.2252	38834.80	3859.78
	,	1.1		-0.2220	39066.00	3917.93
		1.2		-0.2280	37396.09	3725.82
	High (10–120 bar)	I	4300	-0.3216	33929.61	3355.40
	,	1.1		-0.3240	33074.63	3290.99
		1.2		-0.3292	30654.41	2996.32
Parameters	Pressure range	Equivalence ratio	$\delta_{ extsf{L0}}$ [m]		а	Ь
$\delta_{\rm L}$ [m]	Low (I-I2bar)	I	3.9283E-4		<b>-0.4511</b>	-0.8098
	,	1.1	3.6538E-4		-0.4205	-0.8198
		1.2	3.5897E-4		-0.4390	-0.8149
	High (10–120 bar)	1	3.6399E-4		-0.6600	-0.7242
	,	1.1	3.3444E-4		-0.6472	-0.7211
		1.2	3.3757E-4		-0.7616	-0.6989

**Table 2.** Coefficients in the unstretched laminar flame speed (equation (20)) and flame thickness (equation (21)) correlations: curve fits were applied for all the equivalence ratio ranges from 0.4 to 1.8, while results are shown here for only three different equivalence ratios.

# Correlations for the laminar flame speed and flame thickness

When implementing the FES model in the threedimensional simulations, the laminar flame speed and flame thickness are to be used, so correlations were obtained first, as functions of temperature, pressure and equivalence ratio.

The method to generate an appropriate correlation for the unstretched laminar flame speed has been shown in one of our prior papers. The improved Arrhenius form correlation was employed here, as shown in equation (20), where U is a constant,  $\alpha_L$ ,  $\beta_L$ , and  $\gamma_L$  are functions of equivalence ratio, and  $T_0 = 298.15 \, \mathrm{K} \, \& p_0 = 1 \, \mathrm{atm} \, (1.01325 \, \mathrm{bar})$  are the reference temperature and pressure. Here, it should be noted that  $\alpha_L$  and  $\beta_L$  are not related to the  $\alpha$  and  $\beta$  that appeared in equations (18) and (19).

$$S_L = U\left(\frac{T_u}{T_0}\right) \left(\frac{p}{p_0}\right)^{\alpha_L} \exp\left(-\frac{\beta_L}{T_u + \gamma_L}\right)$$
 (20)

A power law correlation was used for the flame thickness, shown in equation (21), where  $\delta_{L0}$ , a, and b are three coefficients all as functions of equivalence ratio only.

$$\delta_L = \delta_{L0} * \left(\frac{T_u}{T_0}\right)^a * \left(\frac{p}{p_0}\right)^b \tag{21}$$

All these coefficients were obtained based on curve fits to the one-dimensional simulation results obtained using CONVERGE, where a wide range of unburned gas temperature (300–950 K), pressure (1–120 bar) and equivalence ratio (0.4–1.8) was covered. Some of the coefficients are presented in Table 2.

It has to be pointed out that:

 To save computational costs in the three-dimensional simulations, an enhanced skeletal model with 48

- species and 152 reactions for iso-octane, developed based on the paper of Liu et al.,<sup>45</sup> was used as the kinetics in the present research, different from the one (874 species and 3796 reactions) used in our prior paper.<sup>46</sup> Thus, the coefficients shown in Table 2 might be different from the referenced paper.
- 2. Two pressure ranges are listed in Table 2, where coefficients for "low" were obtained from one-dimensional cases for pressures of 1 to 12 bar with a step of 1 bar, and "high" for pressures of 10–120 bar with a step of 10 bar. The "low" range would be used to find the unstretched laminar flame speed or flame thickness if the pressure of one numerical cell of interest is below 12 bar, and the "high" range for pressures higher than 12 bar. The behavior is quite different in the low pressure range such that a single correlation covering the entire range was not possible, independent of which kinetics scheme was used.
- 3. Correlations were proposed to represent  $\alpha_L$ ,  $\beta_L$ , and  $\gamma_L$  as functions of equivalence ratio in our prior paper, <sup>46</sup> while in the current study instead, a piecewise linear interpolation based on the local instantanous equivalence ratio was used to find the corresponding coefficients ( $\alpha_L$ ,  $\beta_L$ , and  $\gamma_L$ ). The laminar flame speed calculations for the very rich region (higher than 1.4) need to be included in the current three-dimensional simulations. The very rich region presents different trends from the lower equivalence ratios, and thus was not included in our prior paper. <sup>46</sup>

# **Engine configuration and experimental setup**

Validations for the FES model were provided using a Ford 2017-model-year 4-cylinder 2.0-liter turbocharged gasoline direct injection (GDI) engine in this study.

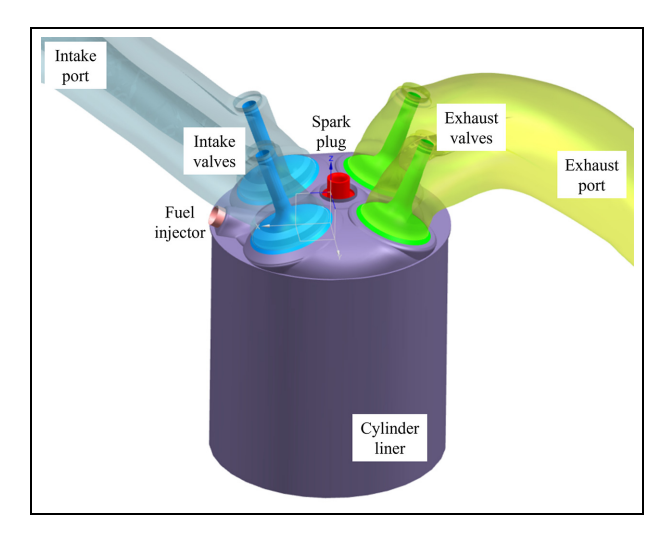


Figure 3. Engine geometry in this research.

The geometry of the engine is shown in Figure 3, with two intake valves and two exhaust valves per cylinder. The engine employed a dual injection strategy during the cold start process, with an early injection happening during the intake stroke to provide a homogeneous background fuel distribution, and a late injection during the compression stroke to provide a rich fuel vapor cloud near the spark plug to ensure successful ignition. A detailed list of the engine configuration is available in Table 3.

The whole system was in an environmental chamber with controlled ambient temperature,  $22^{\circ}\text{C} \pm 1^{\circ}\text{C}$ , throughout the entire set of experiments. A water brake dynamometer was connected to the engine's flywheel to generate a simulated idle load. A National Instruments cRIO system was used to replace the engine control unit (ECU) so that different parameters could be explored to see how each affected cold start hydrocarbon emissions. The in-cylinder pressure for all four cylinders was tracked using a four-channel oscilloscope connected to

the pressure transducer charge amplifiers. The high-resolution transient engine speed was captured and calculated based on the pulse signals of a rotational incremental encoder, which was installed on the flywheel. Unlike the increase in FRP from one cylinder to the next during a typical cold start, for more consistent comparisons among the four events, the FRP was kept constant at 80 and 160 bar in the present cold-start and steady-state experiments, respectively, for all cylinders through external fuel rail pressurization. All the injection duration, so that the total amount of fuel delivered into the engine could be properly controlled. A constant injection profile was used in the simulation within the injection duration.

## Validations for the FES model

## Grid independence analysis

Figure 4 shows the typical cell sizes at the middle cutplane with fixed embedding and AMR used (base grid size: 4 mm). In the vicinity of the spark plug, the cell size near the time of ignition was 0.125 mm, which is larger than many of the scales of turbulence. Thus, the FES model implementation was primarily a subgrid scale (SGS) simulation.

A grid independence analysis was carried out using four different base grid sizes from 2 to 8 mm, and the scaling levels in fixed embedding and AMR were kept the same as shown in Table 1. The pressure traces are compared and presented as the primary vertical axis in Figure 5, where the four cases are shown in different colors. The four curves in Figure 5 perfectly overlap during the compression stroke, while differences can be seen after ignition. The peak pressure increased when the grid size decreased from 8 to 6 mm, and from 6 to 4 mm, while the pressure traces did not vary a lot when the size changed from 4 to 2 mm: the peak pressure

**Table 3.** Engine specifications.

Engine specifications		Details			
		Cold Start	Steady State <sup>a</sup>		
Displacement		1999 cc			
Bore/Stroke		87.5/83.1 mm			
Connecting Rod Length		155.9 mm			
Compression Ratio		10:1			
IVO/İVC		10.9 ATDC/71.1 ABDC			
EVO/EVC		55.1 BBDC/5.1 ATDC			
Injector		6-hole injector			
Fuel Rail Pressure (FRP)		80 bar	160 bar		
Early Injection	SOI	220 BTDC	220 BTDC		
•	duration	2.1 ms for cylinders 3 & 4, 1.7 ms for cylinders 2 & 1	0.95 ms		
Late Injection	EOI	45 BTDC	45 BTDC		
•	duration	2.1 ms for cylinders 3 & 4, 1.7 ms for cylinders 2 & 1	0.95 ms		
Fuel		gasoline			
Firing Order		3-4-2-1			

<sup>&</sup>lt;sup>a</sup>Dual injection strategy was still used for the steady-state measurements in the current research for the model validation.

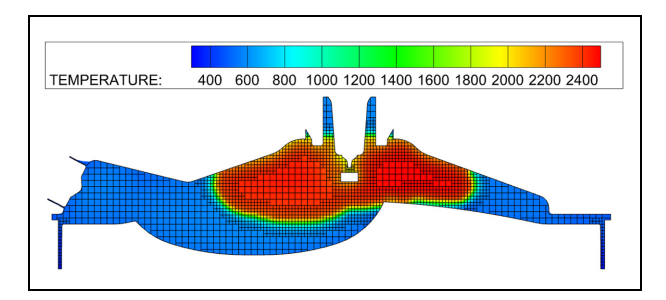


**Figure 4.** Middle cut-plane to show the mesh used in the simulations: fixed embedding and adaptive mesh refinement (AMR) are used; the maximum cell size shown above is I mm; temperature for the background contours.

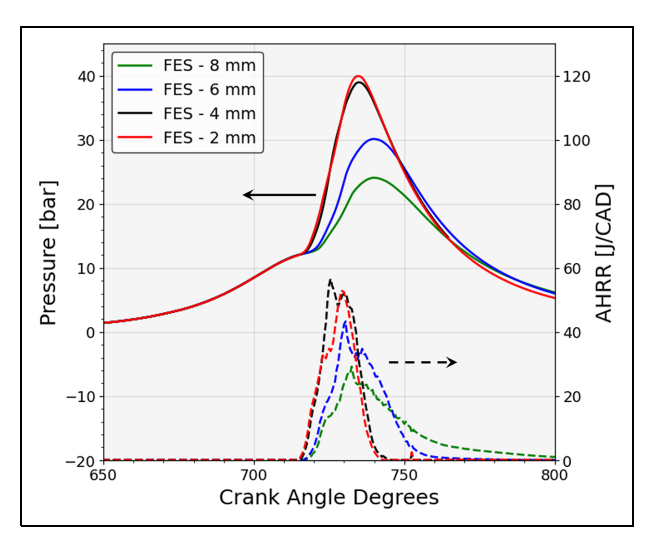


**Figure 5.** Comparisons of cylinder pressure traces for cases with different base grid sizes: 8 mm (green), 6 mm (blue), 4 mm (black), and 2 mm (red); Pressure as the primary vertical axis, and apparent heat release rate (AHRR) as the secondary.

increased by 2.5%; the location of peak pressure (LPP) advanced by 0.2 CA°; and the IMEP decreased by only 0.4%. The differences among different cases mainly originated from the initial combustion, which could be better visualized using the apparent heat release rate (AHRR) curves presented in Figure 5. The AHRR curves for the 4 and 2 mm cases stayed close after the flame was ignited, and increased much faster than the 6 and 8 mm cases. At the early stages of combustion, there was a huge amount of energy delivered into the spark plug gap, igniting the air fuel mixture and making the chemical reaction self-sustaining. The initial flame is small and can be affected by the electrode surfaces of the spark plug. This made it difficult to solve for the first two phases of combustion – kernel formation and early flame growth phases. Thus, a small cell size was essential, and the results converged when the base grid size was reduced to 2-4 mm. Besides, the grid size also had an effect on the simulation in the phase of fully developed turbulent combustion – in particular, there was a deviation for the AHRR curves of 2 and 4 mm cases around 720-730 CAD. However, the overall

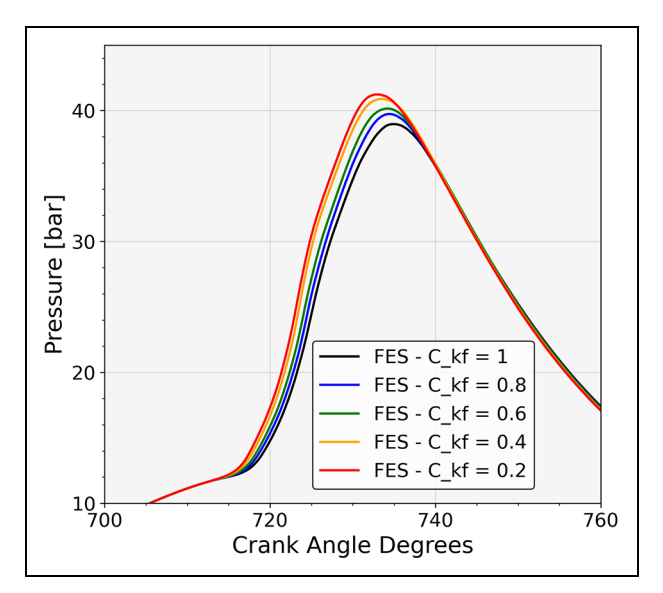


**Figure 6.** Effects of the kernel formation time multiplier  $C_{KF}$  on the simulated in-cylinder pressure history.

effect was not strong for the flame with a large radius and eventually the deviations in pressure traces and IMEP were negligible. Besides, it took about 2 weeks for the 2 mm case, a much longer time, to get the simulation results from the beginning of the simulation to 800 CAD, even though parallel computing was used via our computing center. Therefore, 4 mm was chosen as the base grid size in the simulation cases discussed in the remainder of this paper.

## Effects of kernel formation time

Time is required to wrinkle the flame, so an empirical delay is introduced into the FES model, and the kernel formation time represents the duration of the wrinkling delay. In practical terms, the kernel formation time is the duration from 0% to 2% mass fraction burned. So little thermal energy is released that there is very little effect on the IMEP. However, the duration of this phase affects when the second phase starts. Because the combustion process accelerates during the second phase, any error in predicting the duration of the kernel formation phase affects the phasing of the remainder of combustion. In turn, the error in combustion phasing affects the IMEP. That is, in engine combustion simulations it is very important to predict the kernel formation time accurately.

Cases with different kernel formation times were simulated for cylinder 3 (the first cylinder to fire during the cold start), and the in-cylinder pressure results are shown in Figure 6, where all other parameters were set the same except for the dimensionless multiplier  $C_{KF}$  in equation (8). When the time of the kernel formation was reduced by changing  $C_{KF}$  by a factor of 5 from 1.0 to 0.2, the peak pressure increased by 5.8% and the location of peak pressure (LPP) advanced by 2.0 CA°. The IMEP increased from 6.66 bar for  $C_{KF} = 1$  to 6.72 bar for  $C_{KF} = 0.2$ , an increase of only 0.9%.

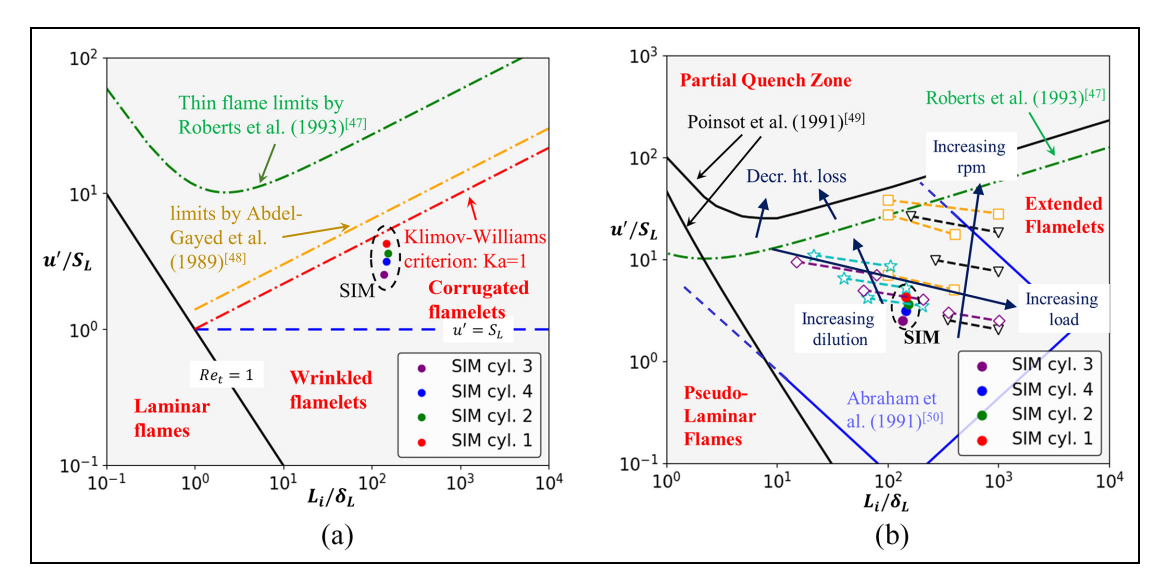


**Figure 7.** Combustion regimes for the four cylinders under cold-start conditions: (a) flame limits proposed by Roberts et al.<sup>47</sup> and Abdel-Gayed et al.<sup>48</sup> and (b) Boghi diagram modified by Poinsot et al.,<sup>49</sup> with estimated engine operating regime by Abraham et al.<sup>50</sup> and engine operating parameters (hollow points) from Matthews et al.<sup>5</sup> and Dai et al.<sup>6</sup>

A variable kernel formation time was used for each of the four cylinders because the engine speed changes during first firing of each cylinder in sequence during the cold start process. Considering that the effects were not obvious, a simple linear function was applied to  $C_{KF}$  which was calculated from the engine speed at the time of ignition for each cylinder:  $C_{KF} = 1$  for cranking engine speed (around 300 RPM) to  $C_{KF} = 0$  for the engine speed at 1500 RPM.

## Predicted combustion regimes

The Borghi diagram, modified by different researchers, shown in Figure 7, is usually used to illustrate the different regimes of turbulent premixed combustion, where the horizontal axis is the ratio of the integral length scale  $(L_i)$  to the laminar flame thickness  $(\delta_L)$ , and the vertical axis is the ratio of turbulence intensity (u') to the unstretched laminar flame speed  $(S_L)$ . Thin flame limits proposed by various researchers 47,48 are shown as dot-dashed curves in Figure 7(a). Four points with different colors represent the simulated values for all four cylinders under cold-start conditions, determined for the flames at TDC of each cylinder. While there is uncertainty regarding the thin flame limits, it appears all four points fall within the regime of corrugated flamelets, and thus the dominant effects of turbulence are to increase the flame surface area and to strain the local flame. Turbulence has no effects on the inner flame structure in this regime, and therefore the flame fronts propagate like laminar flames. As noted previously, these laminar flamelets exhibit fractal characteristics, and it is appropriate to use the FES model to describe the effects of turbulence.

Shown in Figure 7(b) is another Borghi diagram modified by Poinsot et al.,<sup>49</sup> where they defined an

"extended flamelet" as a regime in which the reactants and products are separated by a thin reaction zone that is laminar-like but does not necessarily have the structure of a laminar flame. Different engine operating parameters from Matthews et al.<sup>5</sup> and Dai et al.<sup>6</sup> are presented together as hollow dots, where the effects of engine speed, load, and dilution on the combustion regime are clearly indicated by the arrows.

It is noted that the combustion in the present simulations is shifted toward the thin flame limit as the average engine speed (shown later in Figure 9) increases following the firing order (3-4-2-1). That is exactly the same direction as predicted by the arrow in Figure 7(b) when engine speed increases. The dominant parameter in these four cases is the turbulence intensity (u'), which increases significantly with the average engine speed, while the other three parameters  $(L_i, \delta_L, \text{ and } S_L)$  do not change a lot.

## Results and discussions

## Steady state

The simulation results using the FES model for a steady-state warmed-up condition with a constant engine speed of 1765 RPM ( $C_{KF} = 0$  was used) are compared first with the experimental measurements in Figure 8, where the dual injection strategy was still used in the steady-state tests and the ignition timing was 10 BTDC (see Table 3 for details). The experimental results in Figure 8 represent the average over 300 continuous engine cycles.

The pressure started to increase quickly at about 16 crank angle degrees (726 CAD) after ignition, which was about the same time as the experiments. The incylinder pressure in the simulations increased faster than the experiments at the beginning, though the

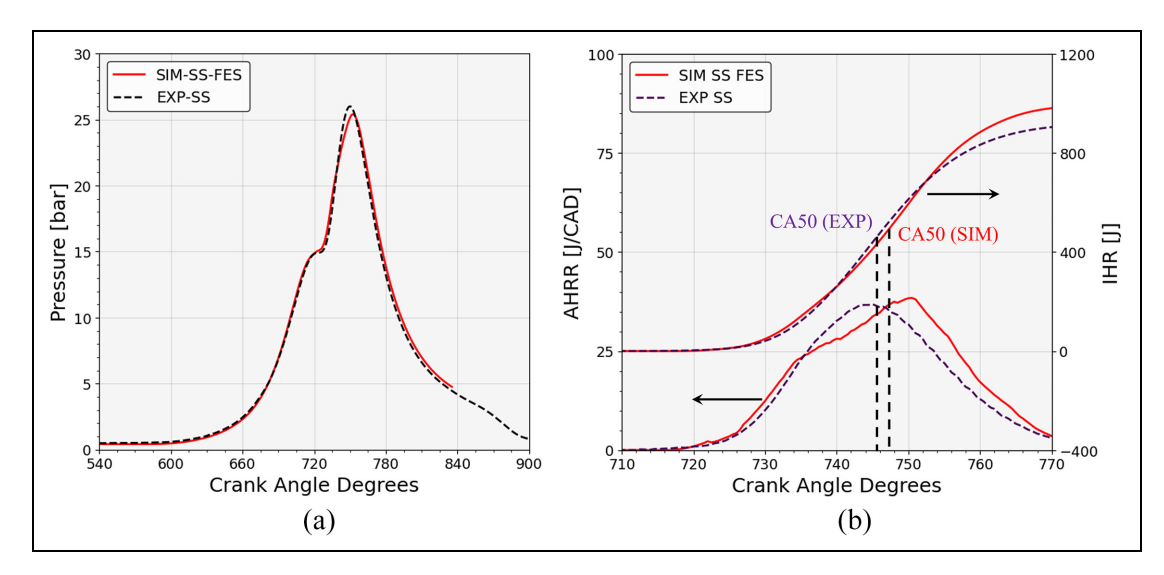
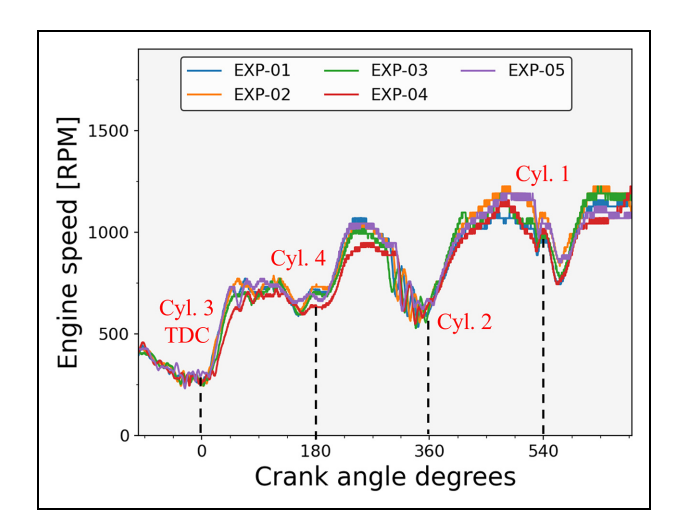


Figure 8. In-cylinder pressure traces (a) and heat release (b) for steady-state conditions: red solid curve for simulation, and dashed curve for the experiments; CA50 marks the crank angle where 50% of the fuel's energy has been released.



**Figure 9.** Engine speeds for the very first firing cycle from five cold-start experiments.

difference was small. The mismatch became more noticeable in the heat release curves presented in Figure 8(b): there is a slightly higher AHRR at the beginning for the simulation compared to the experiments, and then the heat release rate becomes slower later in the simulation; the resulting integrated heat release (IHR) at a late crank angle was higher for the simulation, and the difference in CA50 (the crank angle where 50% of the fuel's energy has been released) is about two crank angle degrees. The main reason for the differences was probably the late injection. For a more consistent comparison with the cold-start simulation, late injection during the compression stroke was also used for the steady-state experiments. The late injection led to an inhomogeneous air-fuel mixture even for the steadystate case, considering there was not enough time for the turbulent mixing with the vaporized fuel. The spatial inhomogeneity of the mixture escalated the engine

cycle-to-cycle variation, making it more challenging for the simulation to exactly match the experiments. Overall, the pressure in both the simulations and the experiments peaked at about 750–752 CAD. The simulated IMEP was 8.33 bar, about 6% higher than that from the experiments. In general, considering the cyclic variability in the experiments, the FES model is predictive for the steady-state conditions and is able to provide comparable results.

More detailed results about how the model behaved for different phases will be presented later in this paper, together with the cold-start results.

## Cold start

As mentioned earlier, the very first firing cycle during the cold start is the focus of our research, and the instantaneous engine speeds from the cold-start experiments are shown in Figure 9. One of these curves was arbitrarily chosen to be used for each of the four different cylinders in the cold-start simulations. The five curves followed the same trend: the engine speed was around 300 RPM before the engine was fired; the engine speed up after ignition in each cylinder and the engine speed increased to about 1200 RPM through the very first firing cycle of all four cylinders.

Pressure traces from five experiments for all four cylinders and the FES results are shown in Figure 10. Unlike Figure 9, where TDCs for different cylinders are presented at different crank angles in a sequential manner, the TDCs of all four cylinders are shifted to 720 CAD in the results shown in Figure 10 for better and easier comparison.

For each individual cylinder, the four experimental curves stayed quite close to each other, while the combustion in one experimental curve was weak compared to the others. This was caused by cyclic variations in the bulk flow, making turbulence levels different in

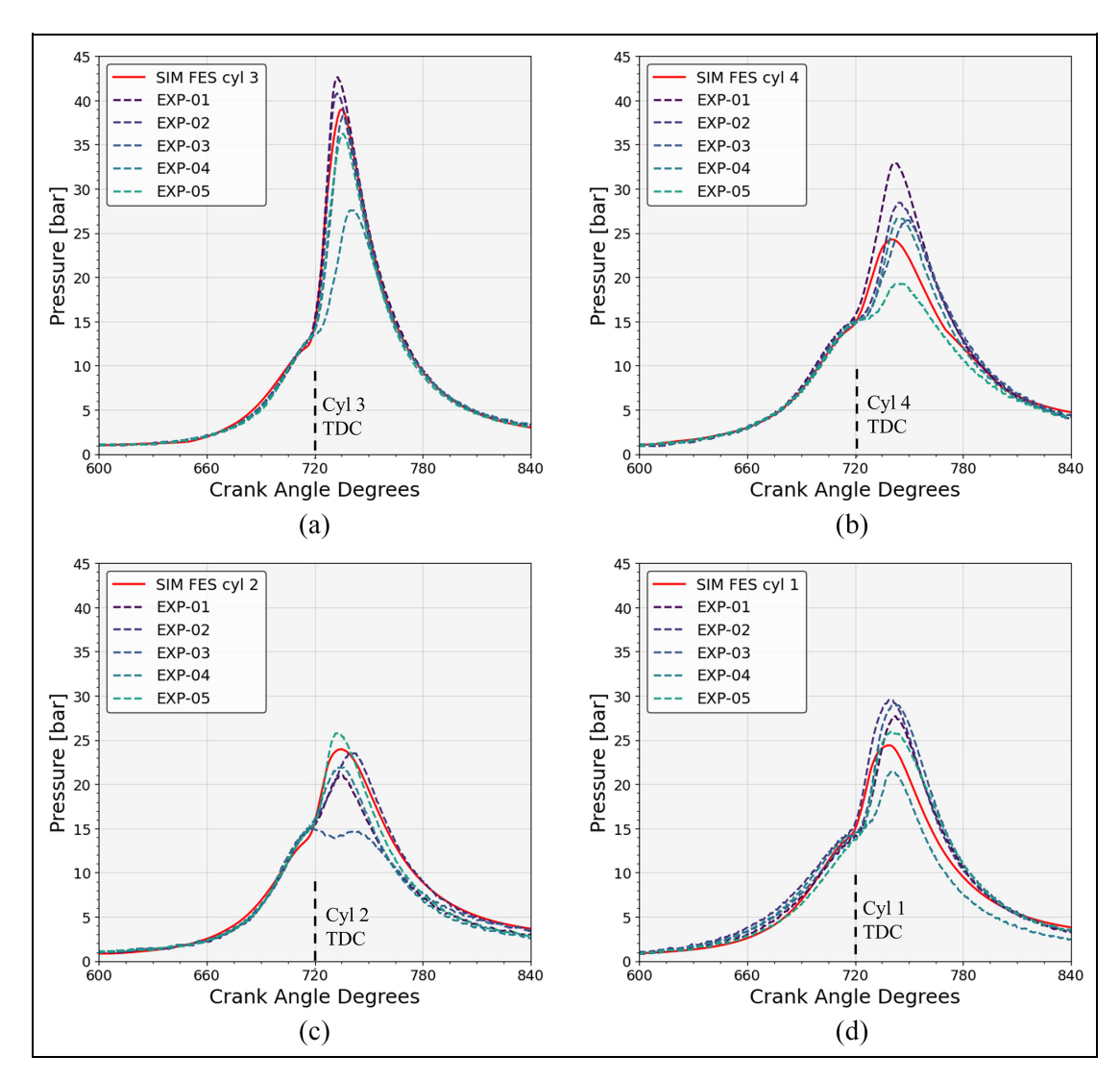
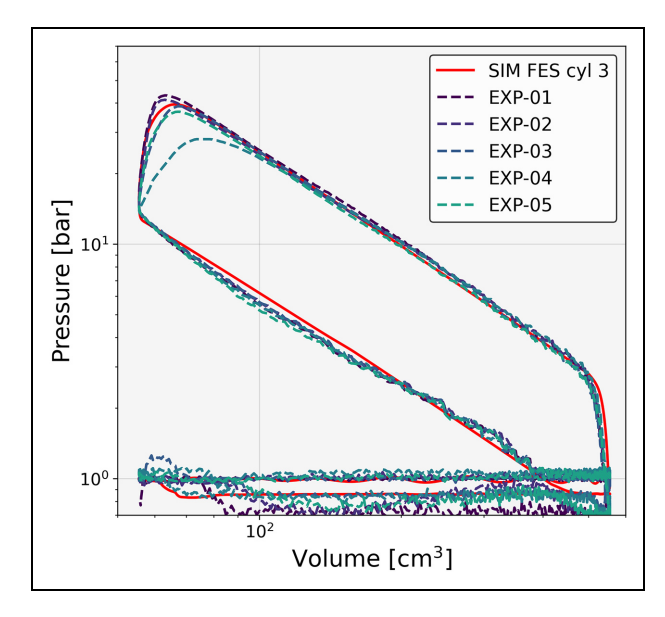


Figure 10. In-cylinder pressure traces for different cylinders: red solid curves for simulation results, and all dashed curves for five different experiments; (a)–(d) for cylinder 3, 4, 2, and 1, respectively, based on the firing order.



**Figure 11.** P-V diagram in logarithmic coordinates for cylinder 3.

different cycles, and thus making the ignition or combustion unstable. The slow evaporation and mixture inhomogeneity from the late injection might be responsible for the day-to-day variation as well. However, the predictions using the FES model will be compared to those robust combustions in the experiments in the present paper.

It is to be noted that there are small deviations between the simulation and experiment pressure traces in Figure 10 for the compression stroke, which we always observed when simulating the first firing cycle and which puzzled us for a long time. This can be better visualized in the P-V diagram shown in Figure 11 for cylinder 3, where the slopes for the experiments and simulation are somewhat different. Later, we realized the difference was caused by the shaft-encoder coupling. We used the encoder to track the engine crank angle, which was installed using a helical-cut flexible shaft coupling between the encoder and the engine crankshaft. The coupling was not perfectly stiff and the

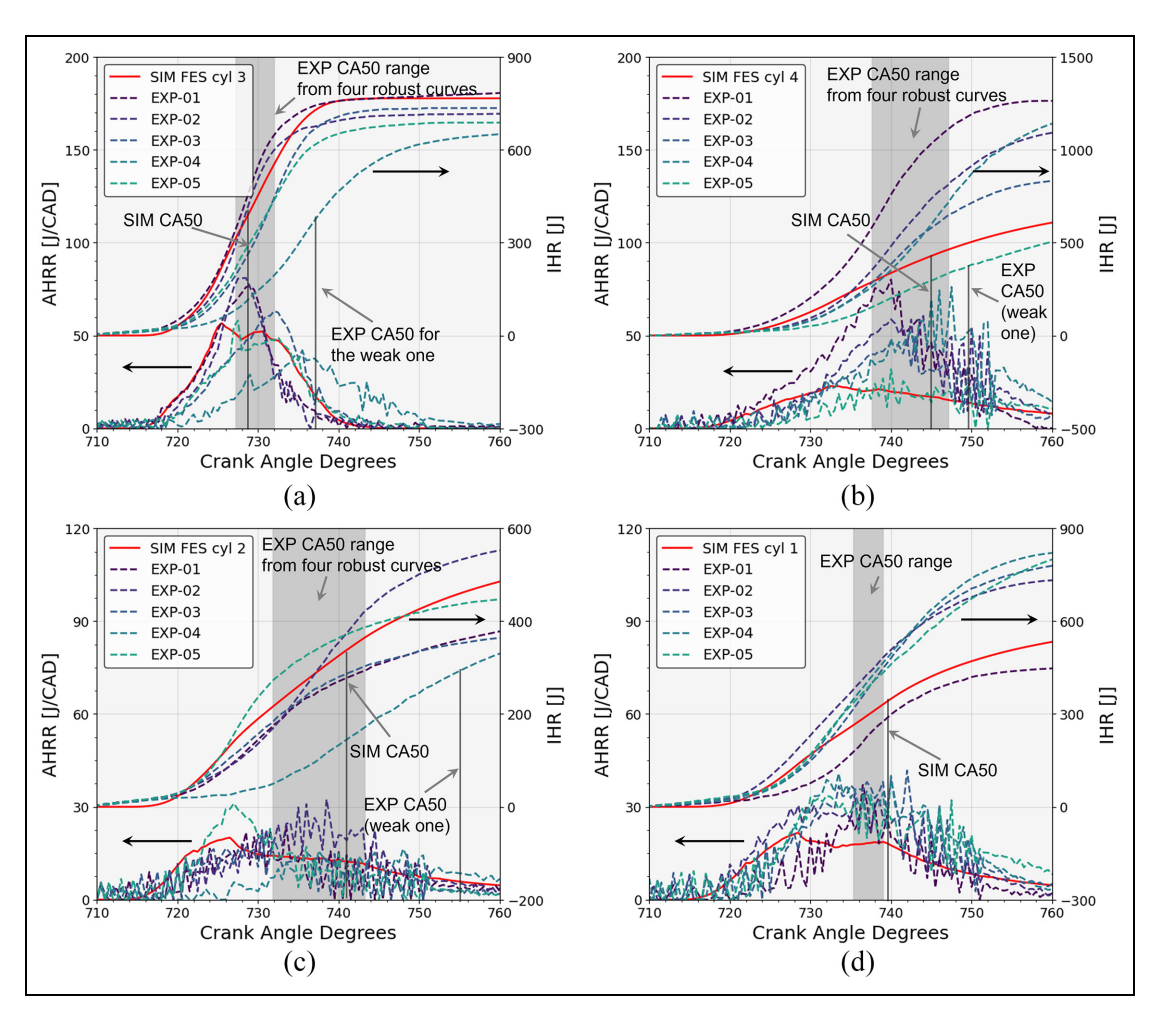


Figure 12. Heat release and CA50 for different cylinders: red solid curves for simulation results, and all dashed curves for five different experiments; (a)–(d) for cylinder 3, 4, 2, and 1, respectively, based on the firing order.

encoder and coupling had rotation inertia as well as compliance. For the very first firing cycle, the engine experienced an instantaneous engine speed transient and hence torque change. This led to some twisting of the encoder coupling that threw off the phasing of the pressure relative to the actual crank angle or distorted the monitored pressure trace. The discrepancy became smaller for cylinder 4 when the engine speed fluctuated within a small range during 45–135 BTDC (Figure 9), and bigger for cylinder 1, the last to fire, when it experienced the greatest change of engine speed. Other evidence for this was that the two curves in the compression stroke were much closer in Figure 8 for the steady-state case. The phasing issue might have caused some deviations in the experimental heat release, IMEP, and location of peak pressure shown below, but the resulting deviations do not exceed the uncertainty in the five experimental traces caused by turbulence and fuel mixture inhomogeneity.

Following Figure 10, the corresponding heat release curves are presented in Figure 12, where the primary vertical axis stands for AHRR, and secondary for IHR. The experimental 95% confidence intervals (detailed values are given in Table 4 shown below) for the CA50s of the four robust-combustion cases are shown as the

shaded areas. All of the initial combustion events matched well with the experiments: although the simulated IHR for each cylinder was a bit low at the very early crank angles, they started their rapid increase around the same time as the dashed curves and the predicted combustion delays matched the experiments. The peak pressures in cylinders 3 and 2, as well as the heat release curves, fell among the four robust combustion curves, whereas they were a little lower for both cylinders 4 and 1, but the differences in peak pressure were only about 3 bar (discussed in more detail in the following paragraph). The simulated CA50s for the first three cylinders lie within or very close to (for cylinder 1) the experimental ranges, indicating an overall agreement of the fully turbulent combustion phase. The trends for combustion in different cylinders appeared the same, strongest in cylinder 3, while relatively weak and close for the other three cylinders.

The 95% confidence intervals were calculated for the magnitude and location of peak pressure, IMEP, and CA50 based on the four robust experimental measurements, and are presented in Table 4. The simulated results for the peak pressure of cylinder 1 and the location of peak pressure (LPP) of cylinders 4 & 1 are outside the confidence intervals and a bit low, but are still

Cylinder number	Peak pressure [bar]		LPP [CAD]		IMEP [bar]		CA50 [CAD]	
	EXP 95% confidence intervals	SIM results	EXP 95% confidence intervals	SIM results	EXP 95% confidence intervals	SIM results	EXP 95% confidence intervals	SIM results
3	35.0–44.0	39.0	731.1–737.1	734.7	6.56–7.59	6.66	727.2–732.0	728.7
4	23.8-33.4	24.3	740.6-749.6	739.7	6.94-8.54	7.62	737.6-747.I	745.5
2	19.7-26.5	24.0	729.6-741.4	734.7	3.36-5.77	5.41	731.8-743.1	741.0
1	25.6-30.6	24.5	738.9-743.4	738.5	5.95-6.89	5.75	735.3-739.0	739.6

**Table 4.** Comparisons for location and magnitude of peak pressure, IMEP and CA50 between experimental measurements and simulations.

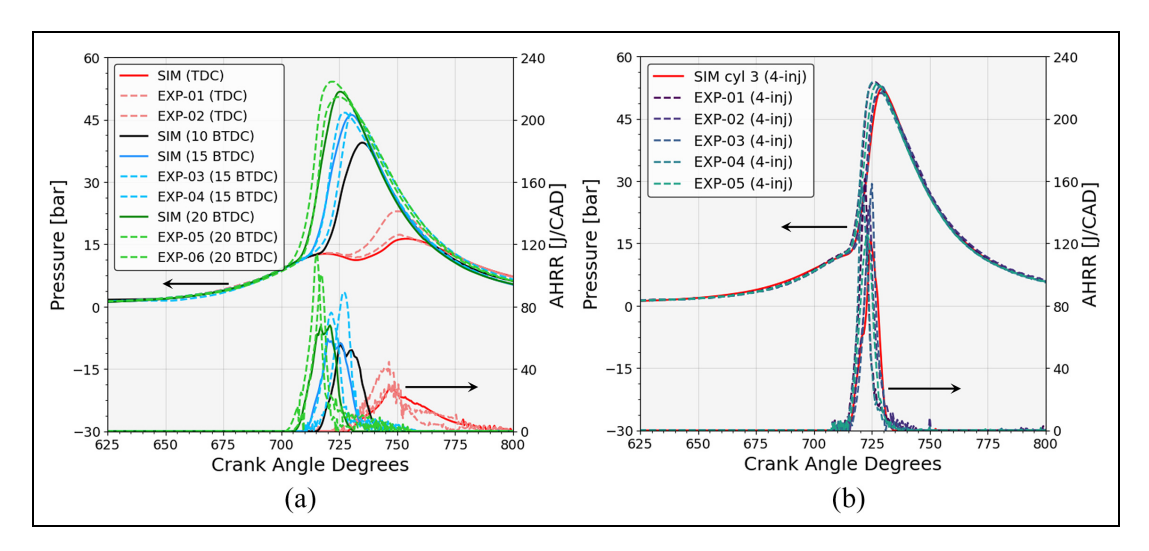


Figure 13. The FES predictions of cylinder 3 for different ignition timings (a) and a 4-inj strategy (b) all solid curves for simulations and dashed curves for experiments; the 10 BTDC curve in (a) is presented for comparison, and details can be found in Figures 10(a) and 12(a).

very close to the lower limits, which also resulted in a slightly lower IMEP for cylinder 1 (3.4% below the lower 95% confidence limit). One possible reason is that late IVC time was used in the experimental strategy, and part of the fuel vapor could flow back to the intake ports before the intake valves were totally closed; based on the firing order (3-4-2-1) and due to the spatial arrangement of the different cylinders, it was easy for fuel to flow back from cylinder 3 to cylinder 4, and from cylinder 2 to cylinder 1; thus the extra fuel vapor could assist the combustion in cylinders 4 and 1 in the experiments, making the actual combustion stronger than in the simulations, wherein the extra fuel was not taken into account for cylinders 4 & 1 simulations.

To show further validations of the FES model, different strategies for the very first firing cycle were simulated for cylinder 3 and are compared with experiments in Figure 13: a sweep of ignition timing from 20 BTDC to TDC is presented in Figure 13(a), where all other engine settings are kept the same as shown in Table 3. For the 4-inj strategy presented in Figure 13(b), the difference is that there are two injections instead of one in the intake stroke with a split ratio of 50:50, and also two injections in the compression stroke with the same split ratio, while the total injected amount stays the same in each stroke.

The pressure traces for the simulations are close to those in the experiments, and discrepancies are more apparent in the AHRR curves, especially for Figure 13(a). There are two peaks in the simulated AHRR curves when ignition is before TDC. The first peak in the simulations always corresponded to the crank angle when the flame front touched the most area of the piston surface, indicating the heat loss to the piston/local extinction played a considerable role. The AHRR curves increased again later when the flame became larger and more volume was involved in the combustion. Actually, the double hump is very common in the cold-start simulations, and can be found in both SAGE and FES models (see Figure A1, and not obvious in Figure 12 since the crank angles are expanded out). However, only a higher but narrower peak exists in most of the experimental AHRR curves, something that we still do not fully understand. The flame-wall interactions are deserving of further examination.

## Different phases in combustion

To show more details about the FES model, the predicted flame radius is presented for all four cylinders in Figure 14(a), where the five solid curves indicate how the flame radius changes in cold-start (labeled as CYL

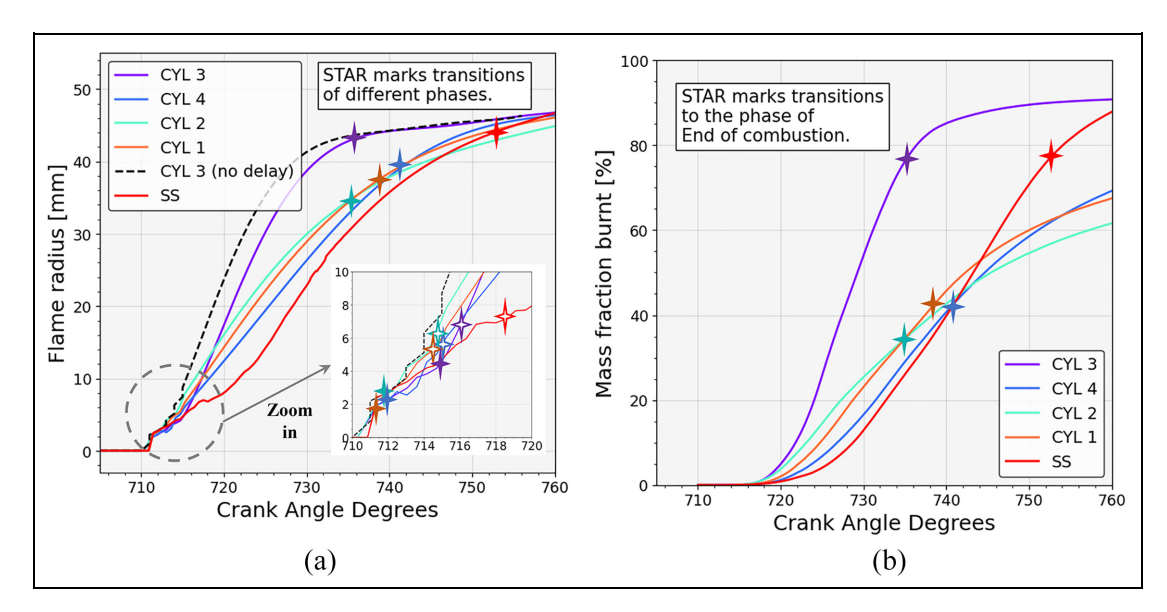


**Figure 14.** Different phases in combustion from simulations: flame radius in (a), stars mark the transitions between different phases of the FES model; mass fraction burnt in (b), stars mark the transitions to the last phase (end of combustion); SS for steady-state, and all others for cold-start in different cylinders.

1–4) and steady-state conditions (labeled as SS), and the stars in the figure mark the transitions between the different combustion phases mentioned above. From those stars, one would know which formulas for the different phases were used to solve the combustion physics at different crank angles. The hollow stars represent the transition between the phase of early flame growth and the phase of fully developed turbulent combustion.

Shown, as well, is the dashed curve for cylinder 3, where there is no "combustion delay" at all, and the formulas in the first two phases are replaced by phase III. It is an imaginary case to show the importance of ignition delay in predictions of the combustion process. It turns out the flame radius increased faster in the nodelay curve right after ignition, and was larger than the normal FES model in the first three phases. Although the duration of the combustion delay looked short in crank angles, it was quite important since the real time in seconds was longer than it appeared when the engine speed was not high, and it would affect the following combustion process.

Figure 14(b) presents the mass fraction burned (MFB) for different simulated cases, where MFB is defined as the fuel mass burned divided by the total evaporated fuel at the corresponding crank angle (considering the gradually evaporating fuel films). The stars label the transitions between the phase of fully developed turbulent combustion and the end of combustion. The transitions for the first three combustion phases are not shown here, since only a small fraction of the fuel was burned during the first two phases, and those can be better visualized in the zoomed-in figure of flame radius (Figure 14(a)). The CA50s discussed earlier were determined with regard to the released energy for comparison with experiments, which may have small differences from the CA50s determined for the

burned mass from Figure 14(b), due to spatial mixture inhomogeneity.

During phase I, the kernel formation phase, there was a sudden increase in the flame radius right after the time of ignition, caused by the breakdown and the following arc phases of the spark ignition (It has to be mentioned that the flame radius information was output every 20 time steps in the simulation, so the rapid jump did not necessarily show up at 710 CAD in the zoomed-in figure). This phase is sometimes referred to as the ignition delay, since so little mass has been burned (Figure 14(b)), and thus, so little energy has been released (Figure 12) that the effect on the cylinder pressure record is slight (Figure 10). The stretched laminar flame speed was used in the FES model to describe the flame propagation in this phase considering its small radius, and to capture the so-called combustion delay. It entered phase II, the early flame growth phase, when the flame became larger but was still smaller than  $L_i$ . The flame radius gradually increased at this moment, and the growth rate was not as fast as phase III, the fully developed turbulent combustion, which was indicated by the increased slope in Figure 14(a). As the flame radius grew, the eddy size which could affect the flame increased as well, until reaching the integral length scale. This led to the two different equations for fractal dimension (equations (10) and (14) and wrinkling scales (equations (12) and (13)) in phases II and III - a gradually increasing characteristic velocity and flame wrinkling scale in the FES model helped capture this turbulence behavior.

Typically, most fuel  $(85\%-90\%^{23})$  is burned before the end of phase III, while our results are lower: less than 80% of the fuel burned for cylinder 3 in cold start and our steady-state measurements, and around 40% for the other three cylinders in cold start. This is related

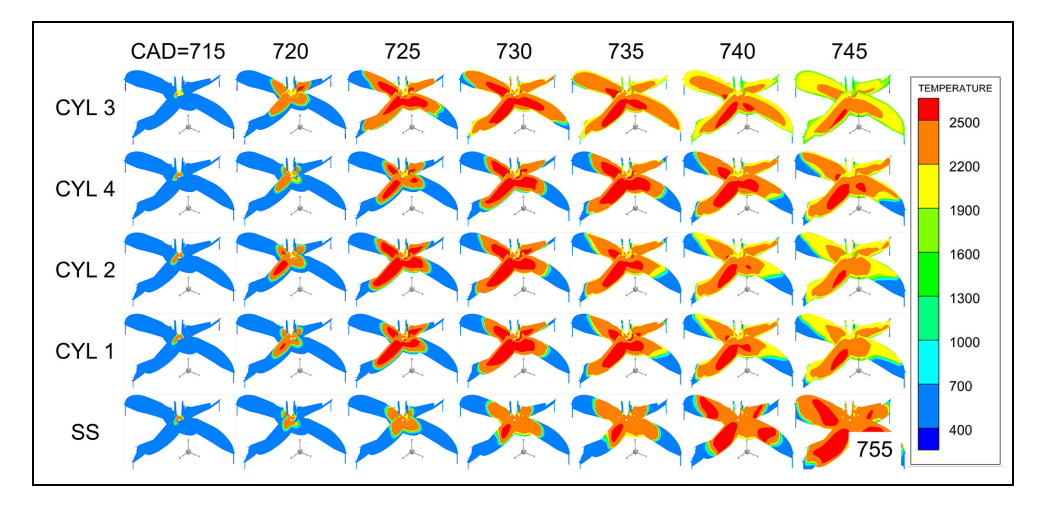


Figure 15. In-cylinder temperature distributions at different crank angles for the cold-start cases (first four rows for four different cylinders) and steady-state case (the last row, where the last contour for 755 CAD).

to the spatial inhomogeneity of the air-fuel mixture, caused by the late injection used in both our cold-start and steady-state cases. The late injected fuel evaporated quickly due to the hot wall for the steady-state warmedup condition. For the first-to-fire, cylinder 3, in the cold-start case, the engine was still at cranking speed, and it allowed a long time for fuel evaporation and turbulent mixing. Thus, in both cases, the MFB results were close to the range of 85%-90%, but still lower due to the stratification. For the other three cylinders in cold-start, they experienced a rapidly increasing engine speed, while the turbulence level was lower under these extremely transitional conditions. Thus, a relatively weak turbulence level and short interval for evaporation enhanced the stratification, resulting in the very slow burning rate.

When the flame interacted with the cylinder wall (around 735 CAD for cylinder 3 of cold-start and 755 CAD for steady-state conditions shown in Figure 15) or with the very lean mixture near the wall (735–740 CAD for the other three cylinders of cold-start in Figure 15), the burning rate began to decrease and the in-cylinder temperature (Figure 15) and pressure (Figure 10) decreased as well. This was when the combustion entered the last phase: end of combustion. The decreasing burning rate in the FES model was associated with either a locally slow flame speed or cooling effects from the walls.

## **Summary and conclusions**

The FES model was integrated into three-dimensional simulations for a GDI engine with a complex geometry in this study, and was used to simulate all four cylinders for the very first firing cycle under cold-start conditions, with transient engine speeds and strong mixture stratification. This paper presents the details of the FES model, including what the formulas are for the four different phases of combustion and how the FES sub-model is integrated into the CONVERGE multi-dimensional

simulation. Validations for both steady-state and coldstart conditions with experimental measurements are provided. Peak pressure, location of peak pressure, heat release, CA50 and IMEP for all four cylinders during the first cycle of cold start are presented and compared, followed by a discussion about the simulated flame radius and MFB in the different phases of combustion.

The primary conclusions from this study are:

- Considering that the effects of turbulence are to wrinkle and stretch the flame in the laminar flame-let regime, fractal geometry is used to relate the turbulent flame speed to the laminar flame speed, where the flame wrinkling scales (L<sub>max</sub> and L<sub>min</sub>) or the ratio of these scales, and the fractal dimension (D) are used to account for the surface area increase due to the flame wrinkling. Different formulas about these parameters are developed for the different stages of combustion. Given the irregular shape of the flame surface, the maximum value of average flame radii on different cross-sectional planes is calculated as the instantaneous flame radius used in the FES model.
- 2. The α- and β- transformations are utilized in a CONVERGE UDF to integrate the FES model into multi-dimensional simulations for the flame zone, and the unburned region is solved by the standard k-ε turbulence model. The improved Arrhenius form correlation is employed to calculate the laminar flame speed and the power law form is used for the laminar flame thickness, both of which are required in the α- and β- transformations.
- 3. An empirical linear correlation, calibrated against experimental measurements, is used to calculate the multiplier  $C_{KF}$  for the prediction of the kernel formation time. A higher peak pressure and an advanced LPP are observed if a smaller  $C_{KF}$  is used, generating a slightly higher IMEP. A more predictive model without the requirement for experimental data to generate a value or values for

CKF is under development to predict the combustion delay. A future paper is planned to present this new model for the kernel formation phase of combustion.

- 4. As indicated by a modified Borghi diagram, the combustion process for all four cylinders under the simulated cold-start conditions fall within the regime of corrugated flamelets, and are shifted toward the thin flame limit as the average engine speed increases following the firing order.
- 5. The close agreement among pressure traces, together with the heat release and MFB curves, validated the equations used for the different phases of combustion for both steady-state and cold-start cases. The additional cases for the very first firing cycle with a sweep of ignition timings and a 4-inj strategy helped verify the capability of the FES model to simulate engine behavior under the cold start transient and with a stratified charge.
- 6. Two peaks were found in the simulated AHRR curves of the cold-start simulations, with the first one caused by the flame front interaction with the piston surface, and the second by either a lean mixture or the cold cylinder walls, while only a higher and shorter peak was observed in the experiments. Further research will be needed to study the flamewall interactions under cold start.

HC emissions are a primary concern for engine cold start, especially for the first several cycles, as mentioned in the introduction section. The simulation results of the fuel tracking using the FES model for the very first firing cycle are presented as the Sankey graphs in another paper<sup>51</sup> of ours, along with experimental measurements. That study showed that there are thick fuel films (26% of total injected fuel) on the cylinder and piston walls at a very late crank angle of the very first firing cycle. However, further examination of the HC emissions was not considered in this study, since the interactions between the fuel and oil films need to be further manipulated in the simulation if that portion is significant to the emissions. Some liquid fuel may be absorbed in the oil and could contribute to the HC emissions once released or evaporated at a later crank angle.

## **Acknowledgement**

We wish to thank CONVERGE CFD™ for providing us with licenses for their simulation software and for their generous technical support. All the simulations shown in this study would not have been possible without the resources and continued support from the Texas Advanced Computing Center (TACC) of the University of Texas at Austin.

### **Declaration of conflicting interests**

The author(s) declared no potential conflicts of interest with respect to the research, authorship, and/or publication of this article.

#### **Funding**

The author(s) disclosed receipt of the following financial support for the research, authorship, and/or publication of this article: this work was supported by Ford Motor Co. through the University of Texas at Austin's Site of the NSF Center for Efficient Vehicles and Sustainable Transportation Systems (EVSTS).

### **ORCID iDs**

Delong Li https://orcid.org/0000-0003-0750-4124 Jinghu Hu https://orcid.org/0000-0001-7465-8161

#### References

- Environment Protection Agency. The 2021 Automotive Trends Report. Report EPA-420-R-21-023, https://nepis.epa.gov/Exe/ZyPDF.cgi?Dockey = P1013L1O.pdf (November 2021, accessed 25 July 2022).
- Rodriguez JF and Cheng WK. Effect of operation strategy on first cycle CO, HC, and PM/PN emissions in a GDI engine. SAE Int J Engines 2015; 8: 1098–1106.
- 3. Hu J, Hall M, Matthews R, Moilanen P, Wooldridge S and Yi J. A novel technique for measuring cycle-resolved cold start emissions applied to a gasoline turbocharged direct injection engine. SAE Int J Adv Curr Prac Mobil 2020; 2(5): 2469–2478.
- Hu J, Hall M, Matthews R, Moilanen P, Wooldridge S and Yi J. Quantitative analysis of gasoline direct injection engine emissions for the first 5 firing cycles of cold start. SAE Tech Paper 2021-01-0536, 2021.
- 5. Matthews RD, Hall MJ, Dai W and Davis GC. Combustion modeling in SI engines with a peninsula-fractal combustion model. *J Engines* 1996; 1105(3): 180–195.
- Dai W, Russ SG, Trigui N and Tallio KV. Regimes of premixed turbulent combustion and misfire modeling in SI engines. SAE J Fuels Lubr 1998; 107(2): 1738–1747.
- Matthews RD. Fundamental combustion modes. Encyclopedia Automot Eng 2014; 1–19. DOI: 10.1002/97811183
  54179.auto115
- Senecal PK, Pomraning E, Richards KJ, et al. Multidimensional modeling of direct-injection diesel spray liquid length and flame lift-off length using CFD and parallel detailed chemistry. SAE Trans 2003; 112(3) 1331–1351.
- 9. Li D, Hu J, Hall M, et al. A simulation study on the transient behavior of a gasoline direct injection engine under cold start conditions. SAE Technical Paper 2022-01–0401, 2022.
- 10. Ravindran AC and Kokjohn SL. The challenges of using detailed chemistry model for simulating direct injection spark ignition engine combustion during cold-start. *Int J Engine Res* 2023; 24: 161–177.
- 11. Ravindran AC, Kokjohn SL and Petersen B. Improving computational fluid dynamics modeling of direct injection spark ignition cold-start. *Int J Engine Res* 2021; 22: 2786–2802.
- 12. Gouldin FC. An application of fractals to modeling premixed turbulent flames. *Combust Flame* 1987; 68(3): 249–266.
- 13. Turbulent burning velocities and flame straining in explosions. *Proc R Soc Lond Math Phys Sci* 1984; 391: 393–414.
- Abdel-Gayed RG, Bradley D, Hamid MN and Lawes M. Lewis number effects on turbulent burning velocity. *Proc Combust Inst* 1985; 20: 505–512.

- North GL and Santavicca DA. Fractal analysis of premixed turbulent flame structure. In: Fall Technical Meeting of the Eastern Section of the Combustion Institute, San Juan, Puerto Rico, 1986.
- North GL and Santavicca DA. Fractal analysis of premixed turbulent flame structure and isovclocity surfaces.
   In: 22nd International Symposium on Combustion, Seattle, August, 1988.
- Murayama M and Takeno T. Fractal-like character of flamelets in turbulent premixed combustion. *Proc Com*bust Inst 1989; 22(1): 551–559.
- Santavicca DA, Liou D and North GL. A fractal model of turbulent flame kernel growth. SAE Trans 1990; 99(3): 90–98. DOI: 10.4271/900024
- 19. Gouldin FC, Hilton SM and Lamb T. Experimental evaluation of the fractal geometry of flamelets. *Proc Combust Inst* 1989; 22(1): 541–550.
- 20. Francke C and Peters N. New aspects of the fractal behavior of turbulent flames. In: 23rd Symposium (International) on Combustion, Orleans, France, 1990.
- 21. Chin Y-W, Matthews RD, Nichols SP and Kiehne TM. Use of fractal geometry to model turbulent combustion in SI engines. *Combust Sci Technol* 1992; 86: 1–30.
- 22. Mantzaras J, Felton PG and Bracco FV. Three-dimensional visualization of premixed-charge engine flames: islands of reactants and products; fractal dimensions; and homogeneity. SAE Paper 881635, 1988.
- 23. Wu C-M, Roberts CE, Matthews RD and Hall MJ. Effects of engine speed on combustion in SI engines: comparisons of predictions of a fractal burning model with experimental data. *J Engines* 1993; 102(3): 2277–2291.
- Matthews RD and Chin Y-W. A fractal-based SI engine model: comparisons of predictions with experimental data. *J Engines* 1991; 100: 99–117.
- Hall MJ, Dai W and Matthews RD. Fractal analysis of turbulent premixed flame images from SI engines. J Engines 1992; 101(3): 1931–1946.
- Hicks RA, Lawes M, Sheppard CGW and Whitaker BJ. Multiple laser sheet imaging investigation of turbulent flame structure in a spark ignition engine. SAE Paper 1994; 103(4): 1463–1482. DOI: 10.4271/941992
- 27. Zhao X, Matthews RD and Ellzey JL. Numerical simulations of combustion in SI engines: comparison of the fractal flame model to the coherent flame model. In: Proceedings of the Third International Symposium on Diagnostics and Modeling of Combustion in Internal Combustion Engines, COMODIA 94, Yokohama, Japan, July 11-14, 1994, pp.157–162. JSME/JSAE.
- Zhu T-T, O'Rourke PJ and Matthews RD. A multidimensional numerical model for turbulent premixed flames with fractal geometries. *J Engines* 1995; 104(3): 2117–2135.
- Matthews R, Roberts C and Ellzey J. SI engine modeling using fractal geometry: promise and prospects. In: 1995 KSEA International Technical Conference and Annual Meeting (KAITCAM) - Globalization and Technology Frontiers, San Francisco, August-September 1995.
- 30. Yoshiyama S, Tomita E, Zhang Z, et al. Measurement and simulation of turbulent flame propagation in a spark ignition engine by using fractal burning model. SAE Paper 2001-01-3603, 2001.
- 31. Suzuki K and Nishiwaki K. Fractal dimension growth in flame front wrinkles during the early phase of flame propagation in an SI engine. SAE Paper 2003-01-1840, 2003.

- Suzuki K and Nishiwaki K. Fractal dimension growth model for SI engine combustion. SAE Paper 2004-01-1993, 2004.
- Baratta M, Catania AE, Spessa E, et al. Development of an improved fractal model for the simulation of turbulent flame propagation in SI engines. SAE Paper 2005-24– 082, 2005.
- Ma F, Li S, Zhao J, et al. A fractal-based quasi-dimensional combustion model for SI engines fuelled by hydrogen enriched compressed natural gas. *Int J Hydrogen Energy* 2012; 37(12): 9892–9901.
- 35. Demesoukas S, Caillol C, Higelin P, et al. Zero-dimensional spark ignition combustion modeling a comparison of different approaches. SAE Paper 2013-24-0022, 2013.
- 36. de Melo T, Machado G and Matias F. Using fractal modeling to predict flex-fuel engine combustion process with different gasoline-ethanol blends. *SAE Paper 2014-36-0162*, 2014.
- Sjeric M, Kozarac D and Taritas I. Experimentally supported modeling of cycle-to-cycle variations of SI engine using cycle-simulation model. SAE Paper 2014-01-1069, 2014.
- Trimbake S, Malkhede D and Devkate P. Combustion characterizations of ethanol/gasoline blended fuel in SI engine using fractal combustion model. SAE Paper 2017-26-0041, 2017.
- 39. Taritas I, Kozarac D, Sjeric M, Sierra Aznar M, Vuilleumier D and Tatschl R. Development and validation of a quasi-dimensional dual fuel (Diesel natural gas) combustion model. *SAE Int J Engines* 2017; 10(2): 483–500.
- De Bellis V, Bozza F and Tufano D. A comparison between two phenomenological combustion models applied to different SI engines. SAE Paper 2017-01-2184, 2017.
- 41. De Bellis V, Malfi E, Teodosio L, Giannattasio P and Di Lenarda F. A novel laminar flame speed correlation for the refinement of the flame front description in a phenomenological combustion model for spark-ignition engines. *SAE Int J Engines* 2019; 12(3): 251–270.
- 42. O'Rourke PJ and Bracco FV. Two scaling transformations for the numerical computation of multidimensional unsteady laminar flames. *J Comput Phys* 1979; 33: 185–203.
- 43. Zhu TT. A multidimensional numerical model for premixed flames with fractal geometries. Ph.D. Thesis, University of Texas at Austin, 1992.
- 44. Moshfeghian M. Correlations for conversion between true and Reid vapor pressures. *Best Tips of the Month* 2018; 20–28. http://www.jmcampbell.com/tip-of-the-month/2016/02/correlations-for-conversion-between-true-and-reid-vapor-pressures-tvp-and-rvp/ (Accessed 8 May, 2023)
- 45. Liu Y-D, Jia M, Xie M-Z and Pang B. Enhancement on a skeletal kinetic model for primary reference fuel oxidation by using a semidecoupling methodology. *Energy Fuels* 2012; 26: 7069–7083.
- 46. Li D, Matthews RD and Hall MJ. Improved correlations for the unstretched laminar flame properties of isooctane/air mixtures. In: Proceedings of the 10th International Conference on Modeling and Diagnostics for Advanced Engine Systems, COMODIA 2022, Sapporo, Japan, July 5-8, 2022, pp.A7-4.
- 47. Roberts W, Driscoll J, Drake M and Goss L. Images of the quenching of a flame by a vortex—to quantify regimes of turbulent combustion. *Combust Flame* 1993; 94: 58–69.

- Abdel-Gayed RG, Bradley D and Lung FKK. Combustion regimes and the straining of turbulent premixed flames. Combust Flame 1989; 76: 213–218.
- 49. Poinsot T, Veynante D and Candel S. Quenching processes and premixed turbulent combustion diagrams. *J Fluid Mech* 1991; 228: 561–606.
- 50. Abraham J, Williams FA and Bracco FV. A discussion of turbulent flame structure in premixed charges. *SAE Trans* 1985; 94: 128–143.
- Hu J, Li D, Hall M, et al. A parametric study to improve first firing cycle emissions of a gasoline direct injection engine during cold start. *Int J Engine Res* 2023; 14680874231153302. DOI: 10.1177/14680874231153302

## Appendix A. Simulation results using the SAGE model

When a relatively high turbulent Schmidt number, 0.78 for example, was used in the SAGE model for cylinder

3, the combustion was weak and the pressure trace was under-predicted, which was similar to what Ravindran and Kokjohn<sup>10</sup> found for the laminar regime, stating: "The SAGE detailed chemistry model ... under-predict the flame propagation speeds." In this study, the turbulent Schmidt number was tuned and eventually set to 0.3 for cylinder 3 to match the experimental pressure traces, and then the same settings were applied in the simulations for the other three cylinders. The final results from the SAGE model are presented as the blue solid curves in Figure A1. The initial combustion events were always too strong in all four cylinders using the SAGE model (see both the pressure and AHRR curves shown in Figure A1), although the peak pressures in cylinders 3 and 4 were at the same level of the experiments. The results using the FES model are shown as well for comparison; detailed discussions about the FES model are provided in the main body of this paper.

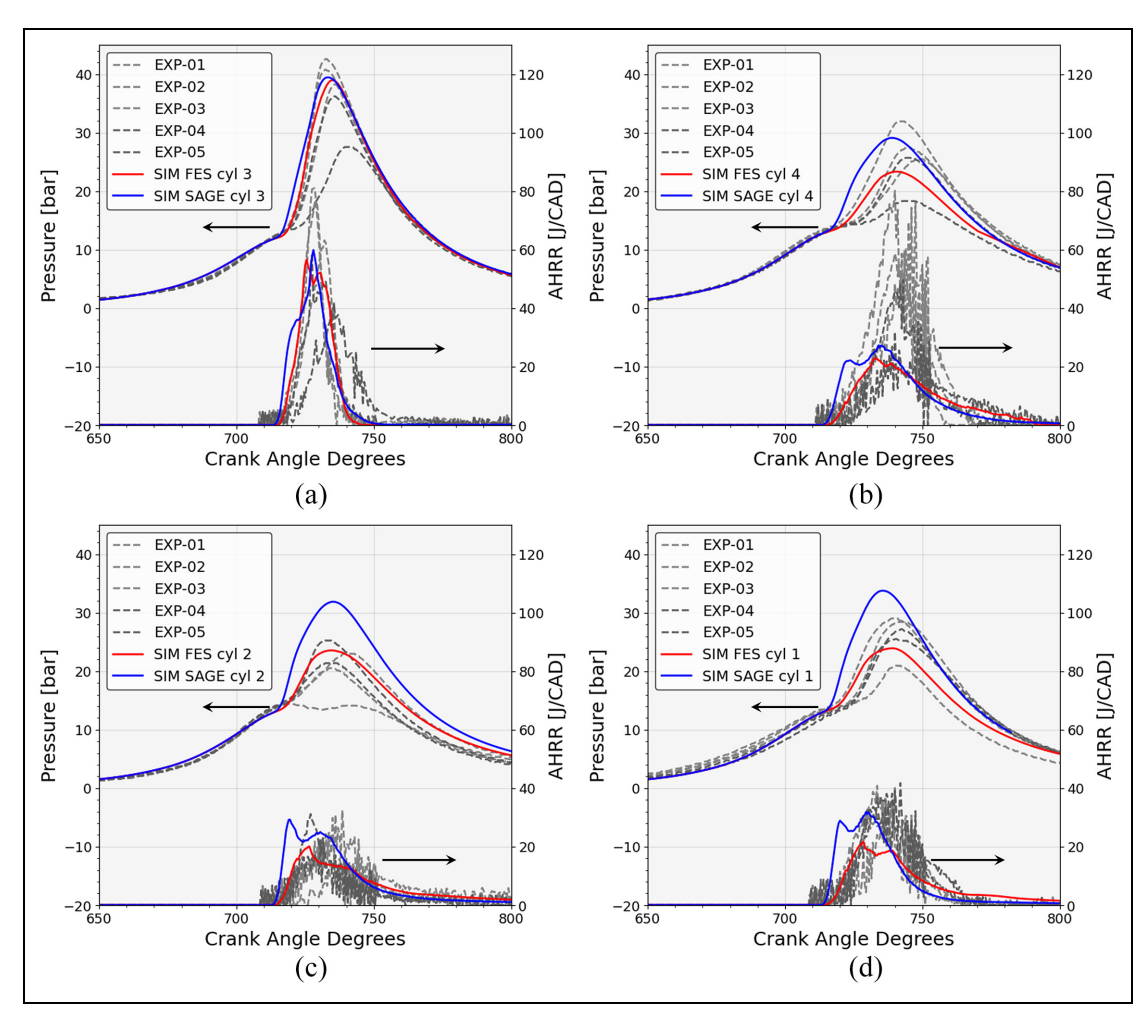


**Figure A1.** In-cylinder pressure traces for the first firing cycles of different cylinders: red solid curves for the predictions using the FES model, blue curves for the SAGE model, and grey dashed curves from cold-start experiments; primary vertical axis for pressure and secondary for AHRR; (a) to (d) for cylinders 3, 4, 2, and 1, respectively.

## Appendix B. Turbulent flame thickness

The turbulent flame thickness was estimated using the temperature profile across the flame. First, we utilized the SAGE model to run a cold start simulation for cylinder 3 in CONVERGE. After tuning the turbulence parameters (the turbulent Schmidt number was set to 0.3, as shown in Appendix A), the temperature distribution was extracted using 200 points along one line across the flame front as shown in Figure B1 (Li1 for intake side and Li2 for exhaust side). Finally, the turbulent flame thickness was calculated based on equation B1, which equals the difference between the maximum temperature (max(T)) and the minimum temperature (min(T)) divided by the maximum temperature slope along the line direction (max( $\frac{\partial T}{\partial x}$ )).

$$\delta_T = \frac{\max(T) - \min(T)}{\max(\lfloor \frac{\partial T}{\partial x} \rfloor)}$$
 (B1)

The turbulent flame thickness was estimated for the flames of both intake (Li1) and exhaust (Li2) sides for two different crank angles (720 and 725 CAD) before the flame front interacted with the cylinder wall. The results ranged from 0.58 to 0.61 mm, and finally 0.60 mm was selected to be used in this model.

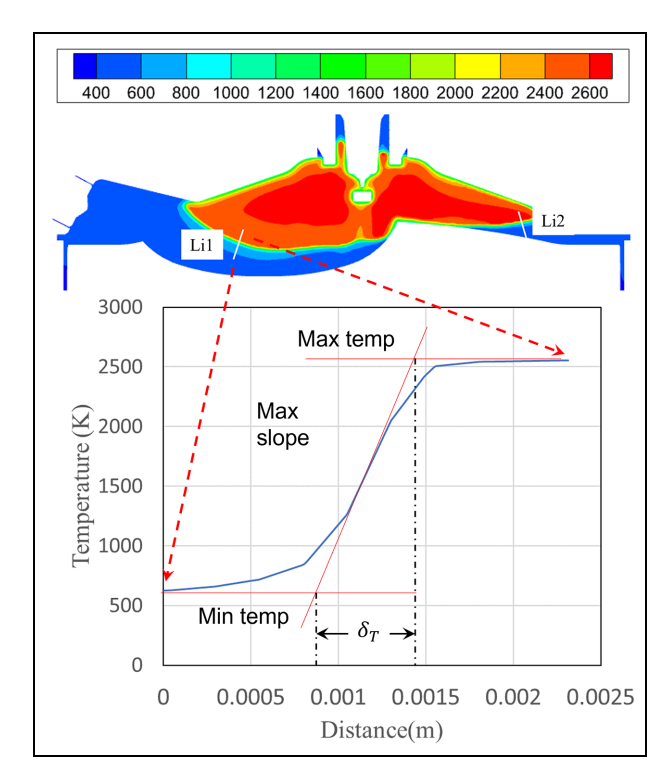


**Figure B1.** Turbulent flame thickness calculation: temperature contour (unit: K) on the middle cut-plane shown here for 720 CAD.